

Imprints of Dark Energy on Cosmic Structure Formation: III) Sparsity of Dark Matter Halo Profiles

I. Balmès*, Y. Rاسera, P.-S. Corasaniti, and J.-M. Alimi

*CNRS, Laboratoire Univers et Théories (LUTH), UMR 8102 CNRS, Observatoire de Paris, Université Paris Diderot,
5 Place Jules Janssen, 92190 Meudon, France*

ABSTRACT

We study the imprint of Dark Energy on the density profile of Dark Matter halos using a set of high-resolution large volume cosmological N-body simulations from the Dark Energy Universe Simulation Series (DEUSS). We first focus on the analysis of the goodness-of-fit of the Navarro-Frenk-White (NFW) profile which we find to vary with halo mass and redshift. We also find that the fraction of halos ill-fitted by NFW varies with cosmology, thus indicating that the mass assembly of halos with perturbed density profiles carries a characteristic signature of Dark Energy. To access this information independently of any parametric profile, we introduce a new observable quantity: the halo sparsity s_{Δ} . This is defined as the mass ratio M_{200}/M_{Δ} , i.e. the ratio of mass inside a sphere of radius r_{200} to that contained within a radius r_{Δ} , enclosing 200 and Δ times the mean matter density respectively. We find the average sparsity to be nearly independent of the total halo mass, while its value can be inferred to better than a few percent from the ratio of the integrated halo mass functions at overdensities Δ and 200 respectively. This provides a consistency relation that can validate observational measurements of the halo sparsity. Most importantly, the sparsity significantly varies with the underlying Dark Energy model, thus providing an alternative cosmological probe.

Key words:

1 INTRODUCTION

In the standard cosmological scenario initial Dark Matter (DM) density fluctuations are the seeds of the cosmic structures we observe today. Gravitational instability amplifies these perturbations that trigger the collapse of the baryonic gas. At early times and on the large scales the dynamics of this process is linear. In contrast at late times and on small scales, as fluctuations grow sufficiently large, the gravitational collapse becomes highly non-linear. It is during this phase that DM particles eventually virialize into gravitationally bounded objects, the halos.

In the hierarchical bottom-up scenario low mass halos form earlier, while massive ones are assembled at later times through mergers of smaller mass halos and accretion of DM particles from the surrounding density field. A complete understanding of this regime is key to disclose the processes that shapes the distribution of matter in the universe. It is inside halos that cooling baryonic gas falls in to form the stars and galaxies that surround us. Moreover, these carry cosmological information that can be tested through galaxy survey observations.

In the future a new generation of survey experiments will probe the nature of the invisible components in the universe through accurate measurements of the clustering of matter on an unprecedented range of scales. This calls for a major theoretical effort

to provide reliable cosmological model predictions. However, because of the complexity of the gravitational collapse, cosmological studies of the DM clustering have mainly relied on numerical N-body simulations.

Numerous works have been dedicated to studying the imprint of Dark Energy on the non-linear cosmic structure formation. In this series of papers we have studied the signature that DE leave on the non-linear matter power spectrum and the halo mass function. In Alimi et al. (2010) we have shown that DE alters the non-linear clustering of Dark Matter at small scales in a very peculiar manner. This is a direct consequence of the fact that DE affects the linear growth of matter density fluctuations and on scales above the stable clustering regime the non-linear collapse carries an integrated record of the past linear evolution (see e.g. Ma 2007). Similarly, the study of the halo mass function in Courtin et al. (2011) has shown that deviations from a universal multiplicity function strongly correlate with the critical density threshold and the virial density predicted by the spherical collapse model of the simulated cosmology. In this paper we specifically focus on the imprint of DE on the density profile of DM halos.

One remarkable result of N-body simulations studies is that Dark Matter halos, regardless of the mass or the characteristics of the underlying cosmological model, exhibit a universal density profile which can be described in terms of a two-parameter fitting formula, the so called Navarro-Frenk-White (NFW) profile (Navarro et al. 1995, 1996). The cosmology dependence is entirely

* E-mail: irene.balmes@obspm.fr

encoded in the relation between the NFW parameters, that is the mass dependence of the concentration parameter. This provides a measure of the compactness of the halo as function of its mass, and has important observational implications, since measurements of the concentration of galaxy clusters can test cosmology and constrain the cosmological parameters.

The mass and redshift dependence of the halo concentration has been studied in a vast literature (see e.g. Navarro et al. 1997; Bullock et al. 2001; Eke et al. 2001; Shaw et al. 2006; Neto et al. 2007; Duffy et al. 2008; Gao et al. 2008; Prada et al. 2012). These studies have focused on the Λ CDM cosmology, while Dolag et al. (2004) first investigated the evolution of the concentration in non-standard Dark Energy models. Their analysis has shown that variations of the concentration-mass relation as function of redshift are related to differences of the linear growth rate of the underlying Dark Energy cosmologies. More recently, De Boni et al. (2013) have found the slope of the $c - M$ relation to be roughly identical in all models, while the normalization depends on the linear growth rate.

Although the emergence of a universal halo density profile is still not understood, a number of empirical studies have suggested that the dependence of the concentration on halo mass and indirectly the appearance of the NFW profile is well correlated with the mass accretion history of halos (see e.g. Wechsler et al. 2002; Zhao et al. 2003, 2009; Ludlow et al. 2013).

On the observational side measurements of the concentration in massive clusters are still far from providing conclusive results (Buote et al. 2007; Schmidt & Allen 2007; Comerford & Natarajan 2007; Okabe et al. 2010; Ettori et al. 2010; Wojtak & Lokas 2010; Oguri et al. 2012). One complication arises from the fact that massive halos may not be relaxed and consequently their profiles may not be smooth. In fact, it is not at all implausible that a large fraction of the most massive clusters consists of unrelaxed halos (Ludlow et al. 2012). Though the profile may depart from the NFW formula (or any other parametric form of the profile) the mass distribution inside such halos still carry cosmological information.

How can we access such information independently of the profile? Does Dark Energy leaves a distinctive signature on halos with perturbed density profiles?

It is the goal of the work presented here to answer these questions. Using a set of numerical N-body simulations of different DE cosmologies we perform a detailed study of the density profiles of DM halos. As a case study, we show that the fraction of halos which are poorly fit by the NFW varies substantially with cosmology. To make use of this effect we introduce the sparsity, an observable measure of the mass distribution in halos which is independent of the halo density profile. We find this to be weakly dependent on the total halo mass, while it carries a distinct imprint of Dark Energy. We show that on a sample of halos the average value of the sparsity is directly related to the halo mass function, thus providing a self-consistent cosmological test applicable to all halos independently of the shape of their profile.

The paper is organized as follows: in Section 2 we briefly describe the cosmological N-body simulations and the algorithms used to perform the numerical analysis; in Section 3 we discuss the halo profile fitting procedure and in Section 4 we present the results of the NFW analysis. In Section 5 we introduce the sparsity and discuss its relevant properties. In Section 6 we describe its use as probe of cosmology and present our conclusions in Section 8.

2 N-BODY SIMULATIONS

2.1 Simulation sets

We use a subset of N-body simulations from the “Dark Energy Universe Simulation Series” (DEUSS) and publicly available through the “Dark Energy Universe Virtual Observatory” (DEUVO) database¹. For more details on these simulations we refer the interested reader to dedicated sections in Alimi et al. (2010); Rasera et al. (2010); Courtin et al. (2011). These have been realized using the adaptive mesh refinement code RAMSES based on a multigrid Poisson solver (Teyssier 2002; Guillet & Teyssier 2011) for Gaussian initial conditions generated using the Zel’dovich approximation with MPGRAFIC code (Prunet 2008) and input linear power spectrum from CAMB (Lewis, Challinor & Lasenby 2000). All simulations have the same phase of the initial conditions.

We consider two class of cosmological models. *Realistic* models, with parameters calibrated against measurements of the Cosmic Microwave Background anisotropies from the *Wilkinson Microwave Anisotropy Probe* (WMAP) 5-year data (Komatsu et al. 2009) and luminosity distances to Supernova Type Ia from the UNION dataset (Kowalski et al. 2008). These models include a standard flat Λ Cold Dark Matter cosmology (Λ CDM-W5) and two quintessence scalar field models characterized by a Ratra-Peebles potential (RPCDM-W5, Ratra & Peebles 1988) and supergravity inspired model (SUCDM-W5, Brax & Martin 2000). *Toy* models are flat cosmological models with different background expansion and linear growth of the density perturbations. We additionally require these models to have the same distribution of linear density fluctuations at $z = 0$, hence the same σ_8 value. These include a large cosmological constant model (L- Λ CDM) with $\Omega_\Lambda = 0.9$, a Ratra-Peebles quintessence model with large value of the slope of the scalar potential (L-RPCDM) and a Cold Dark Matter scenario (SCDM*, the * symbol is to remind that the model parameter values assumed here differ from the SCDM usually considered in the literature; see e.g. Jenkins et al. (1998)). These are used only for the purpose of studying the physical imprint of the underlying cosmological model on the Dark Matter halo profile. We also consider two Λ CDM models best fitting WMAP 1-year (Λ CDM-W1) and 3-year data (Λ CDM-W3) which have nearly identical linear growth histories and mainly differ for the value of σ_8 . For all models the reduced Hubble constant is set to $h = 0.72$, apart Λ CDM-W3 for which $h = 0.73$. The cosmological parameters of the simulated models are listed in Table 1.

We use data from simulations with $162 h^{-1}$ Mpc boxlength and 512^3 particles, and in the case of the realistic models we also use data from simulations with $648 h^{-1}$ Mpc boxlength and 1024^3 particles. The characteristics of these simulations are summarized in Table 2.

2.2 Halo Finder Algorithms

We detect halos using the Spherical Overdensity (SO) algorithm (Lacey & Cole 1994). We estimate the density in each cell by counting the number of particles it contains, then the halo finder starts in the cell with the maximum density. The position of the center in the candidate cell is given by the particle with the largest number of neighbors in a sphere of given radius. The SO finder then draws spheres of increasing radii around that particle. A halo is detected when the density ρ enclosed in a given sphere is Δ times

¹ <http://www.deus-consortium.org/deuvo/>

Table 1. Cosmological parameter values of the simulated models. Ω_{DE} : density parameter for the Dark Energy component; σ_8 : root-mean-square of fluctuations at the 8 Mpc/h scale; α : slope of the potential of the quintessence field; Ω_b : density parameter for the baryons; n_s : scalar spectrum power-law index.

Model	Ω_{DE}	σ_8	α	Ω_b	n_s
Λ CDM-W5	0.74	0.79	0	0.044	0.963
RPCDM-W5	0.77	0.66	0.5	"	"
SUCDM-W5	0.75	0.73	1	"	"
L- Λ CDM	0.9	0.79	0	"	"
L-RPCDM	0.74	0.79	10	"	"
SCDM*	0	0.79	-	"	"
Λ CDM-W1	0.71	0.90	0	0.047	0.99
Λ CDM-W3	0.76	0.74	0	0.042	0.951

Table 2. Parameters of the N-body simulations for the various cosmological models: z_i is the initial redshift, N_{part} is the number of particles in the simulation, L is the simulation boxlength in units of h^{-1} Mpc, m_p is the mass of the particle in units of $h^{-1}M_\odot$ and Δx the comoving resolution in units of h^{-1} kpc. All simulations share the same realization of the initial conditions, and start at high redshift (with $\sigma_{start} \simeq 0.05$ at the scale of the resolution of the coarse grid). Our refinement strategy consist in refining when the number of particles in one cell is greater than 8.

Model	z_i	N_{part}	L	m_p	Δx
Λ CDM-W5	93	512^3	162	2.29×10^9	2.47
"	"	1024^3	648	1.83×10^{10}	9.89
RPCDM-W5	81	512^3	162	2.02×10^9	2.47
"	"	1024^3	648	1.62×10^{10}	9.89
SUCDM-W5	92	512^3	162	2.20×10^9	2.47
"	"	1024^3	648	1.76×10^{10}	9.89
Λ CDM-W1	93	512^3	162	2.55×10^9	2.47
Λ CDM-W3	"	"	"	2.11×10^9	"
L- Λ CDM	"	"	"	8.79×10^8	"
L-RPCDM	"	"	"	2.29×10^9	"
SCDM*	"	"	"	8.79×10^9	"

the mean matter density ρ_m , with Δ the input parameter of the SO halo finder. In contrast, the Friend-of-Friend (FoF) algorithm (Davis et al. 1985) detects halos as group of particles with an intraparticle distance smaller than an input linking-length parameter b . The advantage of this algorithm is that it does not impose any geometrical symmetry on the detected halos, although it tends to link bridged halos. In Appendix A we will show that results on the halo profile and halo sparsity obtained using FoF are in agreement with those inferred from SO halos. On the other hand, we find that relevant differences manifests in the evaluation of the dynamical properties of the detected halos.

Hereafter, we consider only halos with a minimum number of particles of $N_{min} = 1000$. For a fair comparison of the halo properties among the different models we consider the same objects in the different simulations. This task is facilitated by the fact that we have set the same phase of the initial conditions, thus causing structures to form at the same positions in the simulation box.

3 HALO DENSITY PROFILE

3.1 Fitting Procedure

The NFW profile (Navarro et al. 1995) can be explicitly written in terms of the radius r_{200} enclosing an overdensity $\Delta = 200$ relative to the cosmic mean matter density, the enclosed mass M_{200} and the concentration parameter $c = r_{200}/r_s$, where r_s is the scale radius of the halo:

$$\rho_{\text{NFW}}(r) = \frac{M_{200}}{4\pi[\ln(1+c) - c/(1+c)]} \times \frac{1}{r \left(\frac{r_{200}}{c} + r\right)^2}. \quad (1)$$

We fit the NFW formula to each halo in the simulation catalogs and define a χ^2 -statistics as

$$\chi^2 = \frac{1}{N_{\text{bins}}} \sum_{i=1}^{N_{\text{bins}}} \frac{[\rho_i - \rho_{\text{NFW}}(r_i)]^2}{2\sigma_i^2}, \quad (2)$$

where N_{bins} is the total number of concentric shells binning the halo density profile, $\rho_i = n_i/V_i$ is the density in the i -th shell between radius r_{i-1} and r_i , occupying a volume V_i and containing n_i particles; $\sigma_i = \sqrt{n_i}/V_i$ is the Poisson error. We discard all shells that do not contain particles. Since the core of the halo is not well resolved we introduce a cut-off α and fit the NFW profile over the range $(\alpha r_{200}, r_{200})$. To perform the fit we fix the halo mass M_{200} and r_{200} to the values determined by the SO finder and then minimize Eq. (2) as function of the concentration parameter.

Prior to discussing the physical implications of the NFW goodness-of-fit, we test for potential source of errors that may affect the evaluation of the χ^2 . In particular, we find the distribution of χ^2 values systematically vary with the mass resolution of the simulations. To correct for this effect we introduce an alternative measure of the goodness-of-fit and verify that the inferred statistical distribution is independent of the fitting procedure. We limit this analysis to the Λ CDM-W5 model, but we have checked that the results apply to all simulated models.

3.2 Numerical Tests

3.2.1 Mass Resolution

In order to test for the effect of the mass resolution we consider an additional simulation with $162 h^{-1}$ Mpc boxlength and 256^3 particles which has the same mass resolution of the $648 h^{-1}$ Mpc simulation with 1024^3 particles. Halos of same mass in the 256^3 simulation will be less resolved than those obtained in the 512^3 run. Similarly for those in the 1024^3 box compared to the 512^3 case. Hence, in a given mass bin the χ^2 -statistics may vary with the resolution of the simulations, whereas it should be the same. In the left panel of Figure 1 we plot the χ^2 of each SO halos as function of the halo mass M_{200} for the 256^3 (red cross), 512^3 (green cross) and 1024^3 (blue cross) simulations respectively. We can clearly see a systematic trend as function of halo mass and the resolution of the simulations. We find the effect to approximately scale as $\sqrt{N_{\text{part}}}$, where N_{part} is the number of particles in each halo. To correct for this trend we rescale Eq. (2) as

$$\tilde{\chi}^2 = \chi^2 \sqrt{\frac{N_{\text{min}}}{N_{\text{part}}}}, \quad (3)$$

which we plot in the right panel of Figure 1. We can see that $\tilde{\chi}^2$ has absorbed most of the dependence on mass resolution. This can be better seen in Figure 2 where we plot the normalized histogram of χ^2 (left panel) and $\tilde{\chi}^2$ (right panel) for halos in a mass bin

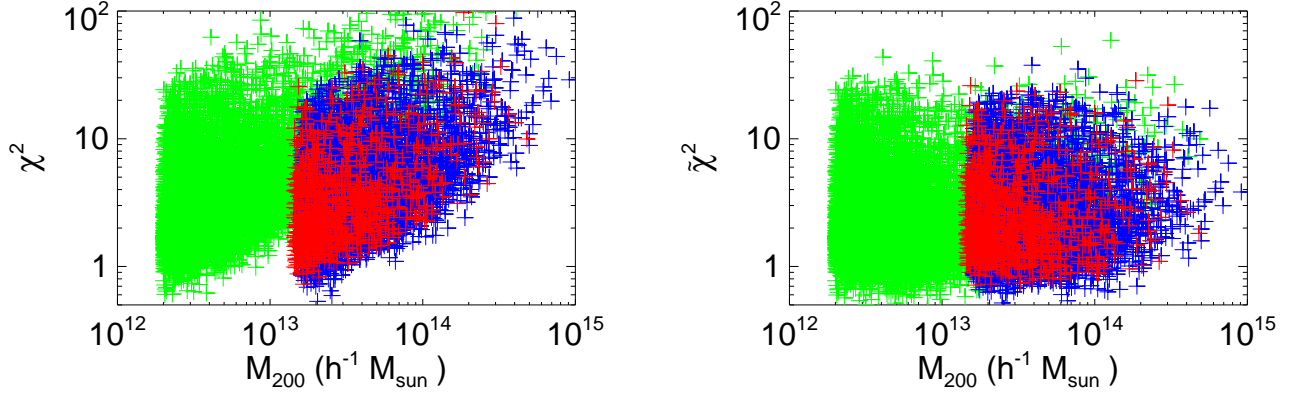


Figure 1. Left panel: χ^2 -values for halos in the 256^3 particle simulation catalog (red cross), 512^3 (green cross) and 1024^3 (blue cross) respectively as function of halo mass. Right panel: same plot for $\tilde{\chi}^2 = \chi^2 \sqrt{N_{\min}/N_{\text{part}}}$ -values. The dependence on the mass resolution has been largely reabsorbed in the rescaling of χ^2 .

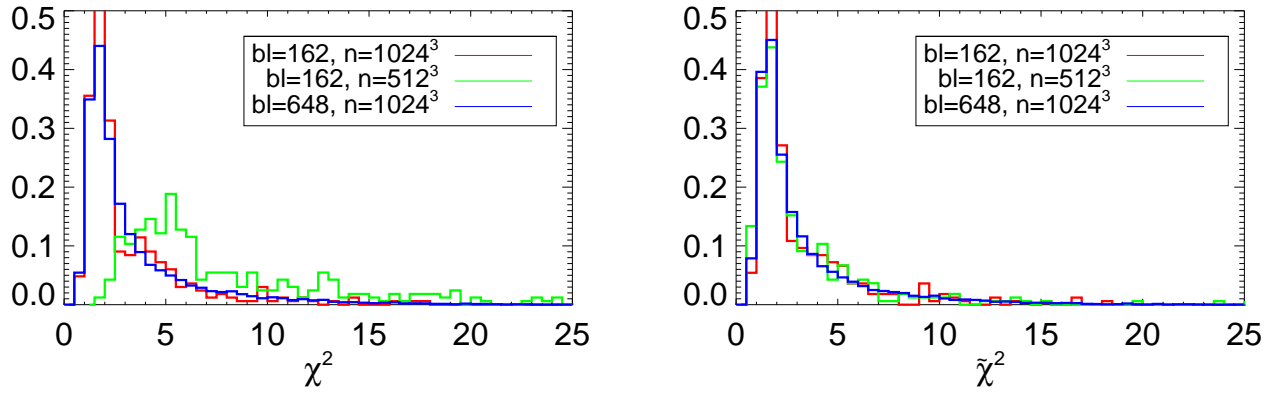


Figure 2. $\tilde{\chi}^2$ -distribution for halos in the mass bin $1.6 \times 10^{13} < M_{200} [h^{-1} M_{\odot}] < 2.0 \times 10^{13}$ from $162 h^{-1}$ Mpc boxlength with 256^3 (red histogram) and 512^3 (green histogram) particles, and $648 h^{-1}$ Mpc boxlength simulation with 1024^3 (blue histogram) particles respectively.

$1.6 \times 10^{13} < M_{200} [h^{-1} M_{\odot}] < 2.0 \times 10^{13}$ which is common to all three simulations. We can see that the probability distribution of χ^2 is identical for the simulations with the 256^3 and 1024^3 particles, while it is different in the 512^3 case. Using the rescaled variable $\tilde{\chi}^2$ the probability distributions are all statistically consistent, though we may notice small differences at the level of the peak and the tail of the $\tilde{\chi}^2$ -distribution for the 512^3 case. This may indicate the presence of some residual mass resolution effects, though differences are less than a few percent, hence smaller than the amplitude of the effects that will be discussed in the next sections and thus negligible. Hereafter, we will use $\tilde{\chi}^2$ as a measure of the goodness-of-fit. However, before proceeding further let us make a few remarks that may help the reader to avoid any confusion related to our definition of $\tilde{\chi}^2$. We have introduced the scaling of χ^2 by $\sqrt{N_{\text{part}}}$ to account for the mass resolution effect, instead we have found convenient to normalize $\tilde{\chi}^2$ such that the lowest mass halos (for which $N_{\text{part}} = N_{\min}$) have the same $\tilde{\chi}^2$ value independently of the simulation mass resolution (this is the $\sqrt{N_{\min}}$ factor in Eq. (3)). Though this may seem arbitrary it does not affect the analysis of the goodness-of-fit. In fact, a different choice of N_{\min} changes the value of $\tilde{\chi}^2$ corresponding to a rigid shift along the y-axis of the points in Figure 1. However, this overall normalization

does not change the shape of the $\tilde{\chi}^2$ -distribution. This is the key point since we do not use the absolute value of $\tilde{\chi}^2$ as indicative of the goodness-of-fit of NFW, but only as a relative measure. As we will discuss next, we are interested in defining populations of halos in terms of their probability of being well fit by NFW and this is quantified by the probability density distribution $\text{Pr}(\tilde{\chi}^2)$ in terms of the relative difference $\Delta\tilde{\chi}^2$ and not the absolute value of $\tilde{\chi}^2$.

3.2.2 Binning and Core Radius

We now consider the effect of varying N_{bins} and α on the goodness-of-fit, using the $162 h^{-1}$ Mpc boxlength and 512^3 particles simulation. As a diagnostic we use the cumulative distribution function

$$Q(\tilde{\chi}_0^2) = \text{Pr}(\tilde{\chi}^2 > \tilde{\chi}_0^2) = 1 - \int_0^{\tilde{\chi}_0^2} \text{Pr}(\tilde{\chi}^2) d\tilde{\chi}^2, \quad (4)$$

which gives the fractional percent of halos whose $\tilde{\chi}^2 > \tilde{\chi}_0^2$.

We have computed $Q(\tilde{\chi}_0^2)$ for several values of N_{bins} with $\alpha = 0.01$ and found no significant variation provided the number of radial bins is sufficiently large, $N_{\text{bins}} > 12$. On the other hand the fitting procedure is more sensitive to the choice of the core radius. We have determined the cumulative distribution for different

Table 3. Values of $\tilde{\chi}^2$ corresponding to 1 and 2 σ deviation from the NFW profile for the simulated cosmologies at $z = 0$ and 1 respectively.

	$z = 0$		$z = 1$	
	1- σ	2- σ	1- σ	2- σ
Λ CDM-W5	3.69	12.00	3.30	8.78
RPCDM	3.82	11.47	3.37	9.08
SUCDM	3.84	11.69	3.33	9.17
L- Λ CDM	4.61	15.39	3.32	9.85
SCDM*	3.05	9.63	3.24	8.74

values of α with $N_{\text{bins}} = 60$. We find that removing a large fraction of the core radius ($\alpha > 0.1$) greatly alters $Q(\tilde{\chi}_0^2)$, while too small values of α result in a fit that is sensitive to the poor resolution of the halo core, thus causing systematically larger values of $\tilde{\chi}_0^2$. We find a good compromise between these competing effects for $\alpha = 0.1$. Thus, for the fitting procedure we consider $N_{\text{bins}} = 60$ bins spaced logarithmically and $\alpha = 0.1$. Hereafter, we will use these values unless specified otherwise.

4 NFW PROFILE AND GOODNESS-OF-FIT

We now focus on the goodness-of-fit of the NFW profile as function of the halo properties, using both the $162 h^{-1} \text{Mpc}$ boxlength, 512^3 particles and the $648 h^{-1} \text{Mpc}$ boxlength, 1024^3 particles simulations. As already mentioned the cumulative distribution function $Q(\tilde{\chi}_0^2)$ is a useful diagnostic since it provides us with a quantitative estimate of the fraction of halos with $\tilde{\chi}^2 > \tilde{\chi}_0^2$. More specifically, from $Q(\tilde{\chi}_0^2)$ we can classify the halo population according to the probability that their profile is fitted by the NFW profile. We find that halos with $\tilde{\chi}^2 \lesssim 3$ are within 1 σ (68% probability) of the NFW profile, while those with $\tilde{\chi}^2 \gtrsim 10$ are poorly fit at more than 2 σ (95.5%). In Table 3 we report the exact value of $\tilde{\chi}_0^2$ corresponding to the 1 and 2 σ limits for each simulated model at $z = 0$ and 1 respectively.

A visual example of this classification is shown in Figure 3 where we plot for the the Λ CDM-W5 model the density profile of nine halos well fit by the NFW at more than 2 σ (left panels), at $\sim 1\sigma$ (middle panels) and poorly fit at more than 2 σ (right panels) with masses corresponding to galaxy (top panels), groups (central panels) and clusters (bottom panels) halos respectively. Halos with mass $M_{200} > 10^{14} h^{-1} M_{\odot}$ are from the 1024^3 simulation, while those with $M_{200} < 10^{14} h^{-1} M_{\odot}$ are from that with 512^3 particles. The red solid line is the best-fit NFW profile in the interval $(0.1 r_{200}, r_{200})$. We may notice that halos with $\tilde{\chi}^2 \lesssim 3$ have profiles that reproduce the NFW formula over the entire radial range. In contrast, halos which depart from NFW at more than 2 σ have profiles that are perturbed especially in the external part ($r > 0.1 r_{200}$) where the slopes deviates multiple times from that of the NFW profile. This is clearly evident in the case of the most massive halo shown in the right bottom panel of Figure 3. The trend inferred from these nine halos is well summarized in Figure 4, where we plot the cumulative distribution for the halos in the 512^3 and 1024^3 particle simulations in the same bins of mass at $z = 0$ (left panel) and 1 (right panel). We can see that for both redshifts $Q(\tilde{\chi}_0^2)$ is systematically shifted to larger $\tilde{\chi}_0^2$ -values for increasing halo masses.

Large deviations from the NFW profile can be related to the distribution of Dark Matter particles that have yet to virialize. As

recently shown by the work of Ludlow et al. (2012), this is more likely to occur in the case of massive halos, which have formed relatively recent and therefore may still be out-of-equilibrium.

Deviations from the virial condition are usually estimated in terms of the parameter $\eta = 2K/|U| - 1$, where K is the kinetic energy and U the potential energy of the halo. However, while there is no ambiguity in the measurement of the kinetic energy associated with halo particles, the computation of the potential energy is much more subtle. This is because U is a non-local quantity, since it also depends on particles that do not belong to the halo, but are in the surrounding density field. Thus, the evaluation of η may be particularly sensitive to the detection algorithm and lead to the definition of a virial selection criterion that strongly depends on the halo finder. In Appendix B we show that indeed the distribution of $\tilde{\chi}^2$ values as function of η strongly depend on the halo detection algorithm. Hence, a rigorous assessment of this problem requires a systematic study that at the moment is still missing. It is beyond the scope of this work to investigate the exact dynamical origin of the deviations from NFW and its relation to the goodness-of-fit. It is reasonable to expect that such a correlation exists, but as shown in Appendix B its significance strongly depends on the halo detection algorithm and the virial selection criteria. However, whether perturbed halo profiles are caused by incomplete-relaxation or dynamical interactions is irrelevant to the point we want to make here. In fact, independently of the dynamical state of halos, it is clear that if NFW is a poor fit to the halo profile then the information encoded in the concentration parameter is uninformative. To show this we plot in Figure 5 the mean halo concentration as function of the total mass for halos which are within 1 σ (green diamonds), 2 σ (orange square) of NFW and ill fitted at more than 2 σ (black circles), error-bars are given by the standard deviation among halos in the same mass bin. We can see that the mean concentration parameter is a monotonically decreasing function of halo mass only for those halos whose profiles is within 2 σ of NFW. This is consistent with the picture that more massive halos form at later times when the mean cosmic density is lower and thus are less concentrated compared to small mass halos which have formed earlier. In Figure 5 we also plot the concentration predicted by Zhao et al. (2009), notice that while this model recovers the mean concentration of halos well fitted by NFW with masses $M_{200} \gtrsim 6 \times 10^{13} h^{-1} M_{\odot}$, at smaller masses it tends to slightly over predict the mean concentration².

In the case of halos ill fitted by NFW at more than 2 σ we can see a very different trend, the mean concentration is small at low masses and increases as function of mass till saturating in the high mass end. Note that the point corresponding to ill-fitted halos at $M_{200} \sim 6 \times 10^{13} M_{\odot}$ encompasses a very small number of halos. That is why we have a large dispersion and discrepancy in the value of the concentration.

We now focus on the cosmological dependence of the goodness-of-fit. To this purpose in Figure 6 we plot $Q(\tilde{\chi}_0^2)$ relative to that of the reference Λ CDM-W5 cosmology for halos at $z = 0$ (left panels) and $z = 1$ (right panels) in the case of toy models (top panels) and realistic ones (bottom panels). We can see that for the toy models at $z = 0$ the fraction of halos with $\tilde{\chi}^2 > \tilde{\chi}_0^2$ relative to the Λ CDM-W5 is larger (smaller) for the L- Λ CDM (SCDM*). Differences are smaller at $z = 1$ especially in the case of the SCDM*; this is not surprising since at higher redshifts the expansion history of Dark Energy models approaches that of the SCDM* model. In

² Throughout this article, we consistently use the mean as opposed to the median usually considered in the literature, see e.g. Zhao et al. (2009)

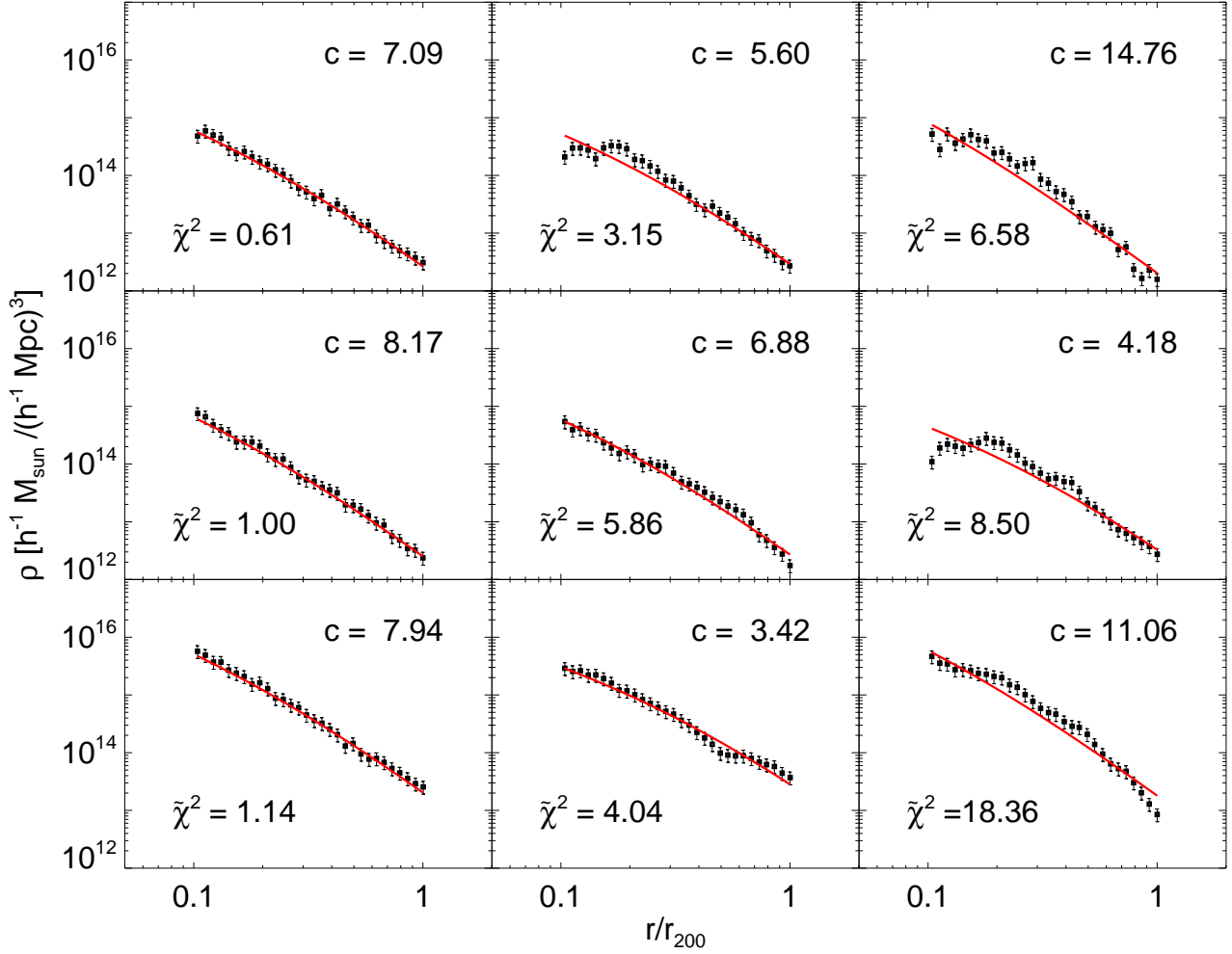


Figure 3. Density profiles of nine randomly selected individual Λ CDM-W5 halos in mass bins $10^{12} < M_{200}(h^{-1}M_{\odot}) < 10^{13}$ (top panels), $10^{13} < M_{200}(h^{-1}M_{\odot}) < 10^{14}$ (middle panels) and $M_{200} > 10^{14} h^{-1}M_{\odot}$ (bottom panels) with $\tilde{\chi}^2$ near the minimum value (left panels), at $\sim 1\sigma$ (central panels) and $\gtrsim 2\sigma$ (right panels) respectively. The red solid line is the best-fit NFW profile in the range $(0.1 r_{200}, r_{200})$.

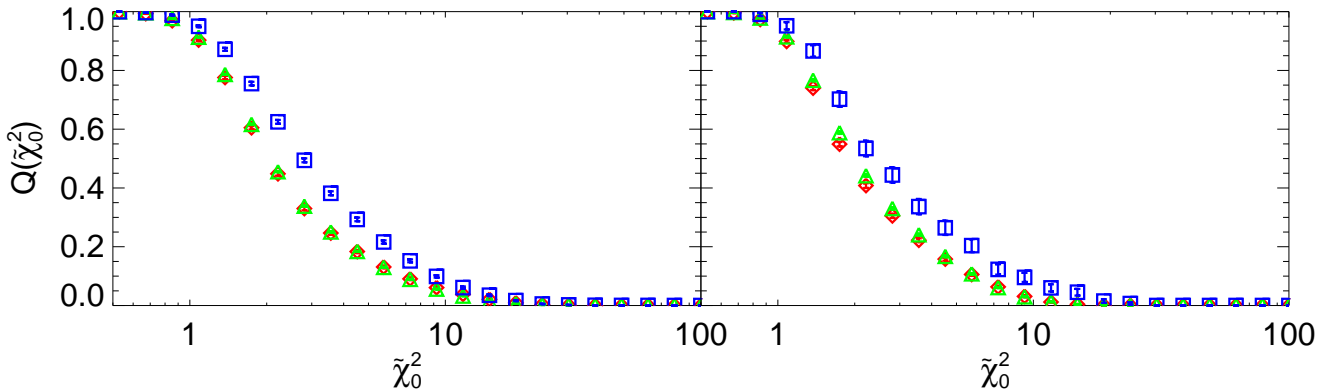


Figure 4. $Q(\tilde{\chi}_0^2)$ for mass bins $10^{12} < M_{200}(h^{-1}M_{\odot}) < 10^{13}$ (red diamonds), $10^{13} < M_{200}(h^{-1}M_{\odot}) < 10^{14}$ (green triangles) and $M_{200} > 10^{14} h^{-1}M_{\odot}$ (blue squares) in the Λ CDM-W5 model at $z = 0$ (left panel) and $z = 1$ (right panel) from the combined halo catalogs of the 512^3 and 1024^3 particles simulations.

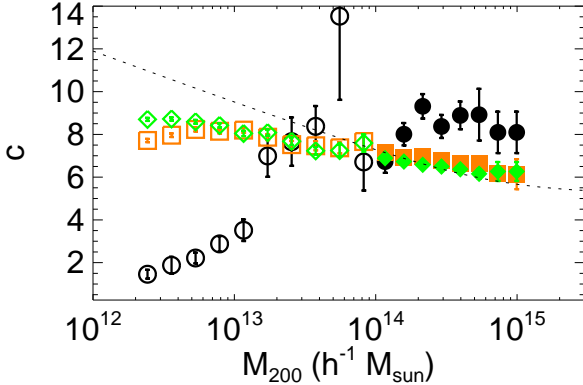


Figure 5. Mean NFW concentration as a function of halo mass for the Λ CDM-W5 model simulation at $z = 0$. Filled symbols correspond to data points obtained from the $648 h^{-1}$ Mpc boxlength simulation with 1024^3 particles, while empty symbols correspond to the $162 h^{-1}$ Mpc boxlength simulation with 512^3 particles. We divide the total subsample in three sub-samples: halos with $\tilde{\chi}^2 < 3$ (green diamonds, fitted by NFW to better than 1σ), halos with $\tilde{\chi}^2 < 10$ (orange squares, fitted by NFW to better than 2σ), halos with $\tilde{\chi}^2 > 10$ (black circles, ill-fitted by NFW at more than 2σ).

the case of the realistic models differences in the cumulative distribution function are smaller than for toy models, again this is not surprising since their expansion histories are calibrated against the same cosmological dataset, nonetheless we can still notice differences $\lesssim 5\%$ at $z = 0$ and of few percent at $z = 1$. This implies that the population of halos which depart from the NFW profile also carry a distinct signature of the underlying cosmological model. As shown in Figure 5, whatsoever the dynamical cause of the perturbed density profile, such information is not correctly encoded in the NFW concentration parameter.

At this point it is reasonable to ask whether assuming a different halo profile fitting formula may lead to different results. Recent studies (see e.g. Ludlow et al. 2013) have shown that “relaxed” halos in N-body simulations are better described by the Einasto profile (Einasto 1965) rather than NFW. The former is characterized by an additional free parameter. However, the improvement of the fit mainly concerns the core region of halos. In contrast, independently of the dynamical state of halos, our analysis highlights deviations from NFW at higher radii, such as those shown in Figure 3, where the Einasto profile closely resembles NFW. Hence, this calls for a characterization of the halo mass distribution that is independent of any parametric fitting formula of the profile.

5 HALO SPARSITY

5.1 Definition

We introduce the halo sparsity defined as the ratio of the halo mass measured at two different overdensities Δ_1 and Δ_2 ,

$$s_{\Delta_1\Delta_2} \equiv \frac{M_{\Delta_1}}{M_{\Delta_2}}, \quad (5)$$

with $\Delta_1 < \Delta_2$. The sparsity provides an estimate of the halo mass excess contained between the radius r_{Δ_2} and r_{Δ_1} relative to the halo mass enclosed in the inner radius r_{Δ_2} . Hereafter, we fix $\Delta_1 = 200$ and let $\Delta_2 = \Delta$ to vary. However, the general properties of the sparsity which will be derived here are independent of the

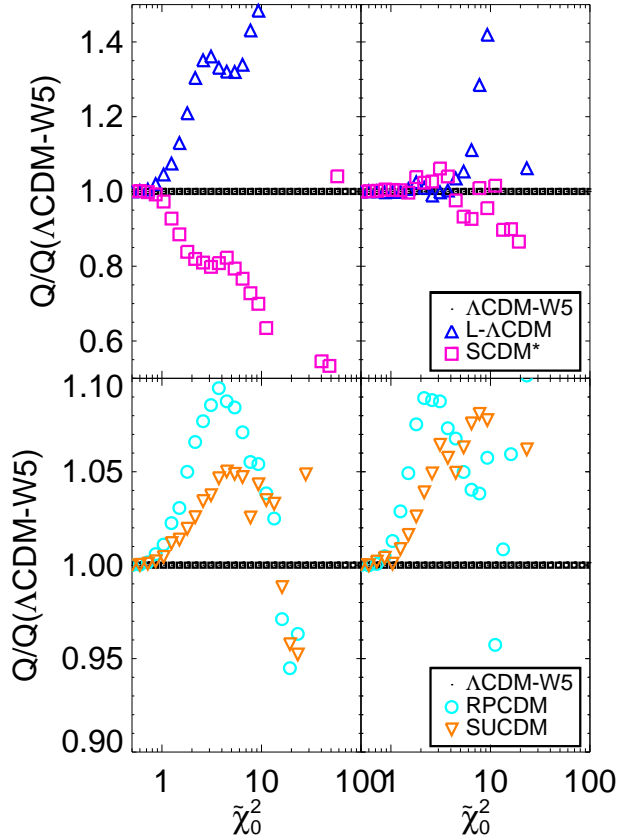


Figure 6. Ratio of $Q(\tilde{\chi}_0^2)$ relative to that of the Λ CDM-W5 cosmology for toy models (top panels) and realistic cosmologies (bottom panels) at $z = 0$ (left panels) and $z = 1$ (right panels) respectively.

specific choice of Δ_1 provided its value is not too small such that the halo retains its individuality. Hence, a lower limit on Δ_1 is probably of order 100. Conversely, Δ_2 cannot be too large, in which case it will be sensitive to mass distribution inside the halo core where baryonic processes, which are not considered here, become relevant. In such a case upper limits on Δ_2 may vary in the range 3000 to 5000 depending on the total halo mass, redshift and cosmology. Notice that the sparsity is a directly measurable quantity that can be inferred from halo mass observational measurements.

At larger overdensities SO halos are characterized by a smaller number of particles, hence in order to be conservative for $\Delta > 200$ we only consider halos with no less than 200 particles.

5.2 Sparsity vs NFW concentration

In the case of halos well fit by NFW the sparsity can be related to the concentration parameter. Let $M_\Delta = \frac{4}{3}\pi r_\Delta^3 \Delta \rho_m$ be the mass enclosed in the radius r_Δ . We can rewrite the sparsity as $s_\Delta = 200/(x^3 \Delta)$, where $x = r_\Delta/r_{200}$, then using the NFW formula we find

$$x^3 \frac{\Delta}{200} = \frac{\ln(1+cx) - \frac{cx}{1+cx}}{\ln(1+c) - \frac{c}{1+c}}. \quad (6)$$

This equation can be solved numerically to find the relation $s_\Delta(c)$, which we plot in Figure 7 for different values of Δ . We can see that

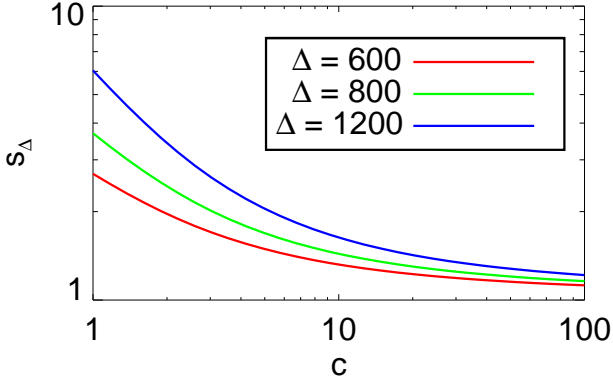


Figure 7. Sparsity as function of the concentration for different overdensity values. The larger the concentration the smaller the sparsity.

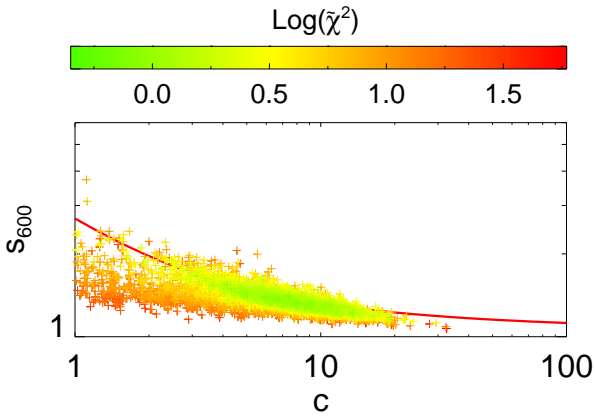


Figure 8. Plot of $s_{600} - c$ for halos in the Λ CDM-W5 cosmology at $z = 0$. The red solid line shows the theoretical prediction for a NFW profile. Many halos depart from this prediction as they are not well described by the NFW profile.

sparsity and concentration are anti-correlated, which explains our choice of dubbing s_{Δ} as sparsity.

In Figure 8 we plot s_{600} as function of the concentration for halos in the Λ CDM-W5 catalog. As we can see halos which are well fit by the NFW profile ($\tilde{\chi}_0^2 < 3$) have a sparsity that is narrowly distributed along the value predicted by Eq. (6). This is clearly not the case for halos whose profile departs from NFW, which is an indication that the concentration parameter (i.e. NFW profile) does not correctly track the mass distribution in the external part of halos between r_{600} and r_{200} . Here, it is worth noticing that over the entire mass range of the halo catalog the sparsity is characterized by a much smaller dispersion than the concentration parameter.

We can reconstruct the halo mass profile by measuring the sparsity at several overdensities and compare it to the NFW prediction. For each halo in our catalog we measure s_{Δ} for $\Delta = \{500, 600, 800, 1000, 1200, 1500, 2000, 3000, 4000, 5000\}$. Then, we use Eq. (6) to derive the corresponding values of $c(s_{\Delta})$ from which we compute the average concentration \bar{c} and dispersion

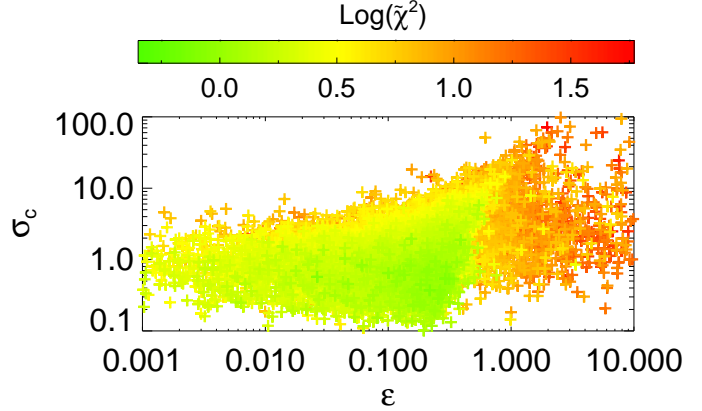


Figure 9. Dispersion about the average value of the sparsity inferred concentration \bar{c} for each halo in the Λ CDM-W5 catalog at $z = 0$ as function of the deviation from the NFW concentration best-fit value, $\epsilon = |\bar{c} - c_{\text{NFW}}|/c_{\text{NFW}}$.

σ_c of each halo:

$$\bar{c} = \frac{1}{N_{\Delta}} \sum_{j=1}^{N_{\Delta}} c(s_{\Delta_j}) \quad \sigma_c = \frac{1}{N_{\Delta} - 1} \sum_{j=1}^{N_{\Delta}} [c(s_{\Delta_j}) - \bar{c}]^2.$$

In Figure 9 we plot σ_c as function of $\epsilon = |\bar{c} - c_{\text{NFW}}|/c_{\text{NFW}}$, where ϵ measures the difference between the average halo concentration of each halo inferred from the sparsity relative to the best-fit value of the NFW concentration parameter. We can see a strong correlation as function of $\tilde{\chi}^2$ and σ_c . In particular, for halos which are well described by NFW, the sparsity inferred concentration \bar{c} coincides with the best-fit NFW concentration parameter to better than a few percent. In contrast, halos with $\tilde{\chi}^2 \gtrsim 10$ are associated with deviation $\epsilon \gtrsim 0.5$ and scatter $\sigma_c \gtrsim 1$. This means that for such halos the NFW concentration is no longer representative of the average compactness of the halo, while the correlation with the large values of σ_c suggests that such deviations are caused by large fluctuations of the mass distribution in halo radial bins.

5.3 Sparsity and Halo Mass

We find the sparsity to be nearly independent of the total halo mass. In Figure 10 we plot the average value of the sparsity as function of halo mass for $\Delta = 500$ (top panel) and $\Delta = 1000$ (bottom panel) respectively with one standard deviation errorbars for halos which are within 1 (green diamonds) and 2 σ (orange squares) of the NFW profiles and ill fitted at more than 2 σ (black circles). For $M_{200} < 10^{14} h^{-1} M_{\odot}$ the sparsity is computed using halos in the 512^3 simulation, while for larger masses we use the 1024^3 halo catalog. We can see that $\langle s_{500} \rangle$ varies less than 5% over the entire mass range, independently of whether the halos are well described by the NFW profile. At low masses the scatter is mainly due to resolution issues since for these halos the number of particles is close to the minimum value of 200. For $\Delta = 1000$ the dependence on the total halo mass is slightly more accentuated especially in the high-mass end with variations $\lesssim 10\%$. In the case of halos ill fitted by NFW the scatter in the value of the sparsity is also within the 10% level, contrary to what was observed for the concentration in figure 5. The high value and dispersion observed for low mass halos is a resolution effect: the mass M_{Δ} is likely underestimated

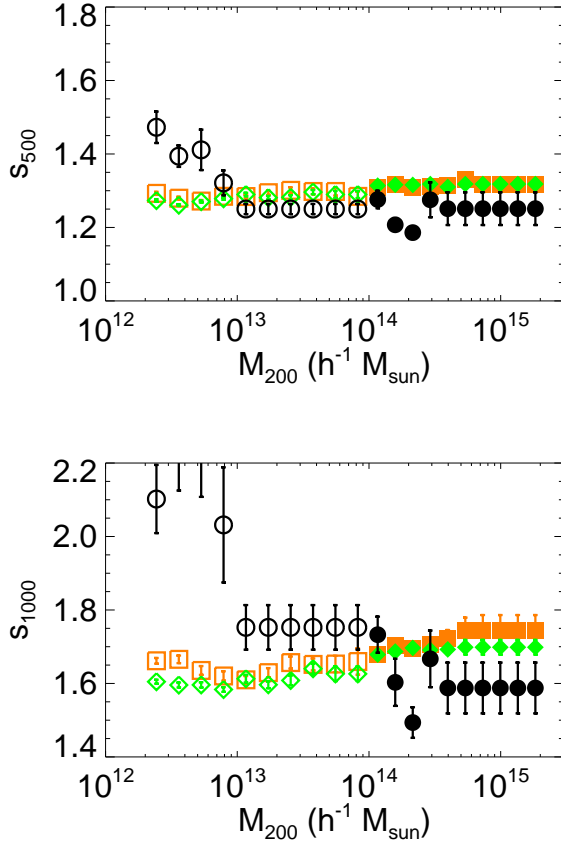


Figure 10. s_{500} (top panel) and s_{1000} (bottom panel) as function of the total halo mass in the Λ CDM-W5 cosmology at $z = 0$. Filled symbols correspond to data points obtained from the $648 h^{-1}$ Mpc boxlength, 1024^3 particles simulation, while empty symbols correspond to the $162 h^{-1}$ Mpc boxlength, 512^3 particles simulation. We divide the total subsample in three subsamples: halos with $\tilde{\chi}^2 < 3$ (green diamonds, fitted by NFW to better than 1σ), halos with $\tilde{\chi}^2 < 10$ (orange squares, fitted by NFW to better than 2σ), halos with $\tilde{\chi}^2 > 10$ (black circles, ill-fitted by NFW). The sparsity for all categories of halos now follows the same trend.

for these halos, as we investigate small radii. This interpretation is consistent with the fact that the discrepancy is larger at higher Δ .

5.4 Halo Sparsity and Mass Function Consistency Relation

Here we show that the average value of the sparsity can be derived from the halo mass function. Let us write the identity

$$\frac{dn}{dM_\Delta} = \frac{dn}{dM_{200}} \frac{d \ln M_{200}}{d \ln M_\Delta} \frac{M_{200}}{M_\Delta} = s_\Delta \frac{dn}{dM_{200}} \frac{d \ln M_{200}}{d \ln M_\Delta}, \quad (7)$$

where dn/dM_Δ and dn/dM_{200} are the mass functions at Δ and $\Delta = 200$ respectively. Since we have shown that s_Δ is nearly independent of mass, the average over the halo ensemble reads as

$$\int_{M_2}^{M_1} \frac{dn}{d \ln M_\Delta} \frac{d \ln M_\Delta}{M_\Delta} = \langle s_\Delta \rangle \int_{\langle s_\Delta \rangle M_2}^{\langle s_\Delta \rangle M_1} \frac{dn}{d \ln M_{200}} \frac{d \ln M_{200}}{M_{200}}, \quad (8)$$

the above relation is transcendental in $\langle s_\Delta \rangle$ and can be solved numerically given the mass function at $\Delta = 200$ and Δ . This implies that knowledge of the mass function at two different overdensities can be used to predict the average value of the sparsity. Vice versa,

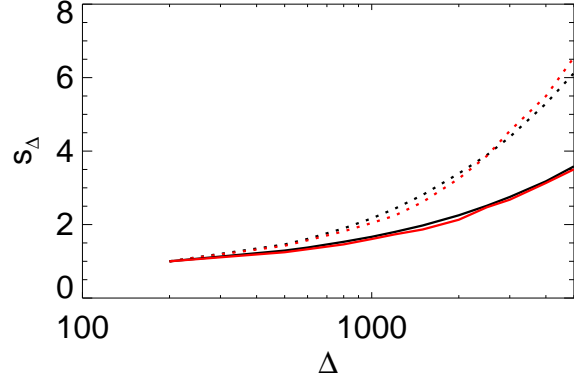


Figure 11. $\langle s_\Delta \rangle$ as a function of Δ at $z = 0$ (solid lines) and $z = 1$ (dotted lines). Black lines correspond to the measured sparsity in the halo catalog, while in red are the mass function based predictions using Eq. (8). Both are in remarkable agreement.

since Eq. (8) involves all potentially observable quantities, it can be used as a consistency test. In fact, let us imagine of observing a sample of clusters for which we measure the mass at two different overdensities, then the inferred mass functions and the ensemble average of the sparsity must satisfy Eq. (8)³.

In Figure 11 we plot $\langle s_\Delta \rangle$ as a function of Δ at $z = 0$ (solid lines) and $z = 1$ (dotted lines) computed from the halos in the Λ CDM-W5 catalog along with the prediction from Eq. (8) using the corresponding halo mass functions at Δ and $\Delta = 200$. We can see that the mass function based predictions work remarkably well at different redshifts and up to large overdensities with residuals $\lesssim 5\%$.

6 COSMOLOGY WITH HALO SPARSITY

We now focus on the imprint of the underlying cosmological model (and specifically of DE) on the halo sparsity.

In Figure 12 we plot the ratio of $\langle s_\Delta \rangle$ relative to that of the reference Λ CDM-W5 model at $z = 0$ (left panels) and $z = 1$ (right panels) for all models listed in Table 1. The bottom panels show a zoom around the Λ CDM-W5 line. We can clearly see that the average sparsity at a given Δ varies from one model to another. We find such differences to be correlated with the linear growth histories of the simulated models as well as the value of σ_8 . For comparison in Figure 13 we plot the linear growth function normalized to its present value as function of the scale factor for the simulated cosmologies. In the bottom panels is shown the ratio with respect to Λ CDM-W5.

Let us first consider the toy models at $z = 0$. We can see that in the case of the SCDM* model the average sparsity is up to $\sim 30\%$ larger than in Λ CDM-W5, while in the case of L-RPCDM and L- Λ CDM this is up to $\sim 30\%$ and $\sim 20\%$ smaller respectively. By construction the toy models have the same σ_8 value. As it can be noticed from the plot in the left panel of Figure 13 the SCDM*

³ A similar consistency test can be inferred by noticing that Eq. (7) can also be written as $\langle s_\Delta \rangle = \langle 1/M_\Delta \rangle / \langle 1/M_{200} \rangle$. Since the sparsity is nearly independent M_{200} then $\langle s_\Delta \rangle = \langle M_{200} \rangle / \langle M_\Delta \rangle$ must be verified. We tested both relations and found them to be in good agreement.

linear growth history is suppressed compared to the Λ CDM-W5, while it is enhanced for L-RPCDM and L- Λ CDM with the former having the largest enhancement. Thus, in the SCDM* case structures form later compared to Λ CDM-W5, hence on average the mass assembled at large overdensities will be smaller, thus resulting in an enhanced average sparsity relative to the Λ CDM-W5. The opposite occurs for L-RPCDM and L- Λ CDM.

Let us now consider Λ CDM-W1 and Λ CDM-W3 cosmologies. These have nearly identical linear growth histories (see Figure 13, right panel), while they have different values of σ_8 . In particular, Λ CDM-W1 has the largest value $\sigma_8 = 0.9$. Because of this, it forms structures earlier than Λ CDM-W5. Consequently, the mass at larger overdensities is greater, which results in a smaller average sparsity compared to that of Λ CDM-W5. In contrast, Λ CDM-W3 has a slightly smaller value of σ_8 , consequently the average sparsity is larger than Λ CDM-W5. In the case of RPCDM and SUCDM, the combined effects of the linear growth history and σ_8 compete to give the differences shown in Figure 12.

These cosmological dependencies are consistent with those expected from Eq. (8). In fact, we can factorize the mass function in terms of the mean cosmic matter density, the derivative of the variance of the linear density field with respect to the mass and the multiplicity function. Since the average sparsity is given by the ratio of the integral of the mass function at two different overdensities, the explicit dependence on the cosmic mean matter density cancels out and remains that on σ_8 and the linear growth factor.

A test of the consistency relation presented in Eq. (8) yields similar results for all cosmological models, with the error being of order a few percent in each case.

These results are consistent with previous findings (see e.g. Dolag et al. 2004; Maio et al. 2006; Ma 2007; Alimi et al. 2010; Courtin et al. 2011; De Boni et al. 2013), namely that the non-linear structure formation still carries a cosmological imprint of the past linear growth history.

Overall, this suggests that the sparsity is a sensitive probe of cosmology. The larger the difference in the integrated linear growth of density fluctuations and/or their normalization amplitude and the larger the imprint on the sparsity.

7 SPARSITY AND HALO MASS MEASUREMENTS

Galaxy clusters are host in massive DM halos. These can be detected with a variety of techniques such as the X-ray emission of the hot intra-cluster gas, the Sunyaev-Zeldovich effects or optical identifications. In recent years numerous survey programs have provided large sample of galaxy clusters up to high redshift (Planck Collaboration 2011; Reichardt et al. 2012; Koester et al. 2007; Menanteau et al. 2012; Pierre et al. 2012). A key aspect of these studies is the measurement of the cluster mass. Under certain hypothesis this can be inferred from locally calibrated scaling relations. Alternatively the cluster mass can be inferred from gravitational lensing observations or measurements of the cluster richness. Each of these methods has its own limitations and is affected by different systematic effects. As an example the hot intra-cluster gas may not be in hydrostatic equilibrium, especially if the cluster is not virialized, this may lead to biased mass estimates. Gravitational lensing measurements may be more reliable as they probe the entire gravitating mass, on the other hand they are affected by mass perturbations present along the line-of-sight.

A measurement of the sparsity requires the halo mass at different overdensities. The range of overdensities that can be probed in a

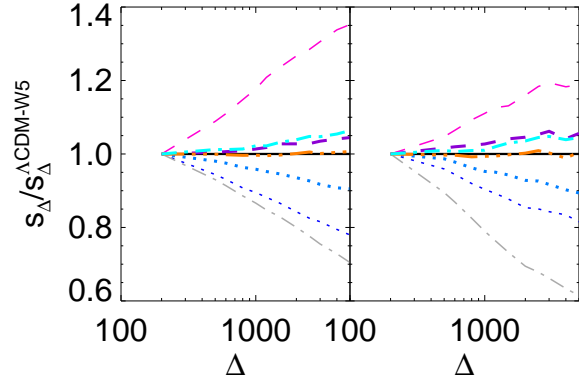


Figure 12. Sparsity of the simulated cosmological models relative to Λ CDM-W5 at $z = 0$ (left panel) and $z = 1$ (right panel) respectively. The bottom panels show a zoom around the Λ CDM-W5 line. The differences, up to 5% even in realistic cosmologies, arise from different structure formation histories.

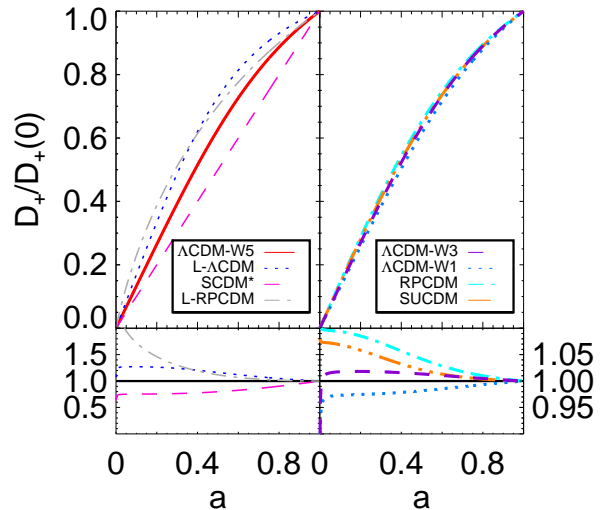


Figure 13. Linear growth rate cosmologies for the toy models (left panels) and realistic cosmologies (right panel). The bottom panels show the relative difference with respect to Λ CDM-W5.

cluster depends on the observational method. As an example X-ray observations cannot probe $\Delta = 200$, while they are more likely to measure the mass at $\Delta = 500$. Higher overdensities require sufficient angular resolution. The inferred value of the sparsity can then suffer of systematic uncertainties affecting the mass measurements. Nevertheless, the existence of the sparsity consistency relation shown in Eq. (8) on a large cluster sample can provide an effective diagnostic for testing unknown systematics.

To give an illustrative example of the cosmological relevance of the sparsity we compute the average value from a sample of 30 clusters around $z \sim 0.2$ from Okabe et al. (2010) (see table 1 of this article for the redshifts and table 8 for the 2D masses) for which lensing mass estimates at overdensities $\Delta_c = 112$ and $\Delta_c = 500$ with respect to the critical density have been obtained without assuming a NFW profile. These are 2D projected masses and in principle we should compare it to the sparsity of 2D halo masses from our catalogs. However, if we assume the halos to be

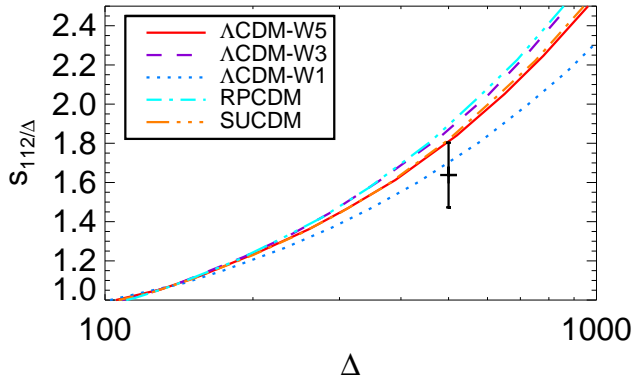


Figure 14. Comparison of the average sparsity of a cluster sample with 2D lensing masses from Okabe et al. (2010) against predictions from the simulated cosmological models. The overdensity Δ quoted here is with respect to the critical density.

approximately spherical, and given the fact that we study the ratio of two masses, we expect the differences to be minimal. The average sparsity of the cluster sample is $\langle s_{112,500} \rangle = 1.71 \pm 0.38$ which we plot in Figure 14 together with the simulated cosmological model predictions. The latter have been obtained by converting the N-body halo mass measurements with respect to the critical density using the relation $\Delta_c = \Omega_m \Delta (1+z)^3 / E^2(z)$, where $E^2(z) = (1 - \Omega_m) + \Omega_m (1+z)^3$ in the case of a flat universe (having neglected the contribution of radiation). In this proof-of-concept, we use the simulations at $z = 0$ to compare with the observations at $z \sim 0.2$ since we lack the simulation snapshots at the correct redshift.

As we can see even a single estimate of the sparsity can potentially have a significant constraining power and which is worth to further investigate in future work.

8 CONCLUSIONS AND PERSPECTIVES

In this paper we have studied the imprint of DE on the density profile of DM halos using a set of halo catalogs from the DEUSS project. We have shown that the goodness-of-fit of the NFW profiles varies with mass, redshift and cosmology. In particular, the fraction of halos ill fitted by NFW systematically varies with the underlying cosmologies. Thus, the mass distribution in such halos still carries cosmological information.

We have introduced the halo sparsity to retrieve the DE dependent signature encoded in the mass distribution inside all halos independently of a parametric profile. We have shown that the average value of the sparsity is related to the halo mass function at different overdensities and we have inferred a consistency relation that can be used either to predict its value if the halo mass functions are known or validate observational measurements of the sparsity.

In the future large sample of galaxy clusters from multi-wavelength observations can be used to infer accurate measurements of the sparsity from which it will be possible to derive alternative cosmological constraints.

ACKNOWLEDGEMENTS

I. Balmès is supported by a scholarship of the “Ministère de l’Éducation Nationale, de la Recherche et de la Technologie” (MENRT). The research leading to these results has received funding from the European Research Council under the European Community’s Seventh Framework Programme (FP7/2007-2013 Grant Agreement no. 279954). This work was granted access to the HPC resources of CCRT and IDRIS under allocations made by GENCI (Grand Équipement National de Calcul Intensif).

REFERENCES

- Alimi, J.-M., Füzfa, A., Boucher, V., Rasera, Y., Courtin, J., Corasaniti, P. S., 2010, *MNRAS*, 401, 775
- Brax P., Martin J., 2000, *Phys. Rev. D*, 61, 103502
- Bullock, J. S., et al., 2001, *MNRAS*, 321, 559
- Buote, D. A., et al., 2007, *ApJ*, 664, 123
- Comerford, J. M., Natarajan, P., 2007, *MNRAS*, 379, 190
- Courtin, J., Rasera, Y., Alimi, J.-M., Corasaniti, P. S., Boucher, V., Füzfa, A., 2011, *MNRAS*, 410, 1911
- Davis, M., Efstathiou, G., Frenk, C. S., White, S. D. M., 1985, *ApJ*, 292, 371
- De Boni, C., Ettori, S., Dolag, K., Moscardini, L., 2013, *MNRAS*, 428, 2921
- Dolag, K., et al., 2004, *A&A*, 416, 853
- Duffy, A.R., Schaye, J., Kay, S. T., Dalla Vecchia, C., 2008, *MNRAS*, 390L, 64
- Einasto, J., 1965, *Trudy Inst. Astroz. Alma-Ata*, 51, 87
- Eke, V., Navarro, J., Steinmetz, M., 2001, *ApJ*, 554, 114
- Ettori, S. et al., 2010, *A&A*, 524, A68
- Gao, L., et al., 2008, *MNRAS*, 387, 536
- Guillet, T., Teyssier, R., *J. Comput. Phys.*, 2011, 230, 4756
- Jenkins, A. et al., 1998, *ApJ*, 499, 20
- Koester, B., et al. 2007, *ApJ* 660, 221
- Komatsu, E., et al. 2009, *ApJS*, 180, 330
- Kowalski M. et al., 2008, *ApJ*, 686, 749
- Lacey, C., Cole, S., 1994, *MNRAS*, 271, 676
- Lewis A., Challinor A., Lasenby A., 2000, *ApJ*, 538, 473
- Ludlow, A. D., et al., 2012, *MNRAS*, 427, 1322L
- Ludlow, A. D., et al., 2013, *MNRAS* in press, arXiv:1302.0288
- Ma, Z. 2007, *ApJ*, 665, 887
- Maio, U., et al., 2006, *MNRAS*, 373, 869
- Menanteau, F., et al. 2012, arXiv:1210.4048
- Navarro, J. F., Frenk, C. S., White, S. D. M., 1995, *MNRAS*, 275, 720
- Navarro, J. F., Frenk, C. S., White, S. D. M., 1996, *ApJ*, 462, 563
- Navarro, J. F., Frenk, C. S., White, S. D. M., 1997, *ApJ*, 490, 493
- Neto, A. F., et al., 2007, *MNRAS*, 381, 1450
- Okabe, N., et al., 2012, *PASJ*, 62, 811
- Oguri, M., et al., 2012, *MNRAS*, 420, 3213
- Pierre, M., et al., 2011, *MNRAS* 414, 1732
- Planck Collaboration 2011, *A&A* 536, 28
- Prada, F., Klypin, A. A., Cuesta, A.J., Betancort-Rijo, J. E., Primmack, J., 2012, *MNRAS*, 423, 3018
- Prunet, S., Pichon, C., Aubert, D., Pogogyan, D., Teyssier, R., & Gottloeber, S. 2008, *ApJs*, 178, 179
- Rasera, Y., et al., 2010, *AIP Conf. Proc.* 1251, 1134
- Ratra, B., & Peebles, P. J. E. 1988, *Phys. Rev. D*, 37, 3406
- Reichardt, C. L., et al., 2012, arXiv:1203.5775
- Schmidt, R. W., Allen, S. W., 2007, *MNRAS*, 379, 209

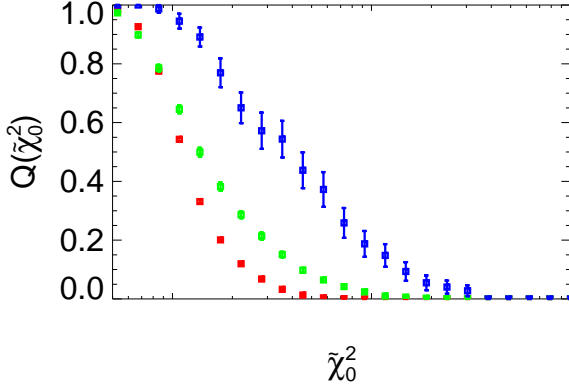


Figure A1. $Q(\tilde{\chi}_0^2)$ for FoF halos at $z = 0$ in different bins of mass.

- Shaw, L. D., Weller, J., Ostriker, J. P., Bode, P., 2006, *ApJ*, 646, 815
 Teyssier, R., 2002, *A&A*, 385, 337
 Wechsler, R. H., Bullock, J. S., Primack, J. R., Kravtsov, A. V., Dekel, A., 2002, *ApJ*, 568, 52
 Wojtak, R., Lokas, E. L., 2010, *MNRAS*, 408, 2442
 Zhao, D. H., Jing, Y. P., Mo, H. J., Borner, G., 2003, *ApJ*, 597, L9
 Zhao, D. H., Jing, Y. P., Mo, H. J., Borner, G., 2009, *ApJ*, 707, 354

APPENDIX A: FOF HALOS

In this Appendix we briefly present the results on the halo profiles obtained from halos detected with the FoF algorithm with $b = 0.2$. The purpose is to show that the results on the NFW goodness-of-fit and the halo sparsity do not depend on the precise identification criterion of halos. Here we restrict ourselves to the results obtained with the $162 h^{-1}$ Mpc boxlength and 512^3 particles simulation. Note that the mass indicated for halos is M_{200} , i.e. the mass obtained by constructing a sphere of overdensity 200 around the density peak of the structure found by the FoF algorithm. We fit the density profile of FoF halos using the same procedure used for SO ones, and use $\tilde{\chi}^2$ to evaluate the goodness-of-fit.

Figure A1 shows the cumulative distribution function, $Q(\tilde{\chi}_0^2)$, obtained from FoF halos respectively for three different bins of mass. This figure is to be compared with the left panel of Figure 4. The dependence on the halo mass is more important for FoF halos, possibly due to a remaining dependence of the goodness-of-fit on the mass resolution. Surprisingly, FoF halos seem to have a generally lower $\tilde{\chi}^2$ value than SO halos, especially at small masses. This is likely due to the rescaling factor we apply to χ^2 to account for resolution effects. A more careful study is needed to determinate the appropriate scaling in the case of FoF halos.

In Table A1 we list the values of $\tilde{\chi}^2$ corresponding to 1 and 2σ deviations from the NFW profile. For SO halos, we have obtained values around 3 and 10 respectively, while in the case of FoF halos these are around 1 and 3.

In Figure A2 we plot the halo sparsity at $\Delta = 500$ and 1000 respectively for both SO and FoF halos, we can see that the results are remarkably similar.

Table A1. Values of $\tilde{\chi}^2$ corresponding to 1 and 2σ deviation from the NFW profile for FoF halos in the simulated cosmologies at $z = 0$ and 1 respectively.

	$z = 0$		$z = 1$	
	1σ	2σ	1σ	2σ
Λ CDM-W5	1.49	3.86	1.55	3.16
RPCDM	1.56	4.05	1.62	3.31
SUCDM	1.51	4.06	1.56	3.19
L- Λ CDM	1.70	4.68	1.49	3.29
SCDM*	1.42	3.16	1.63	3.26

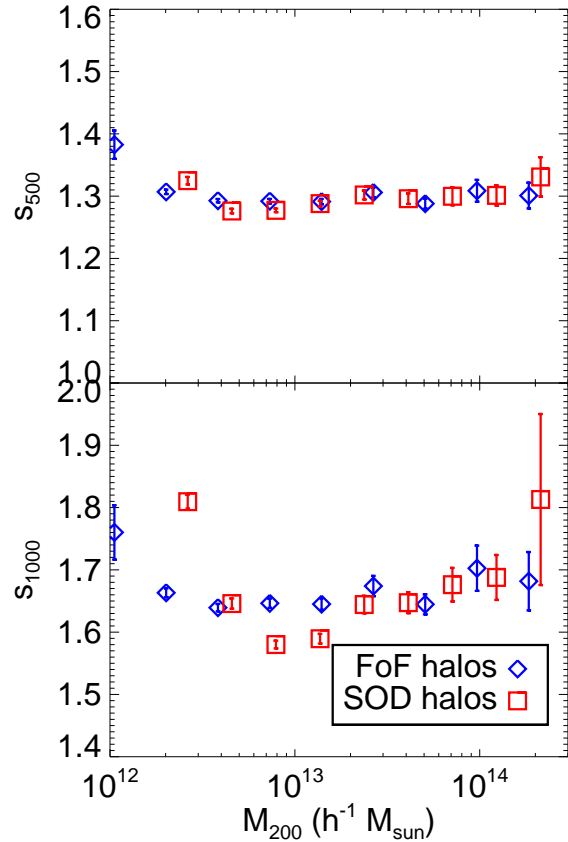


Figure A2. Comparison of s_{500} and s_{1000} derived from FoF and SOD halos in Λ CDM-W5.

APPENDIX B: GOODNESS-OF-FIT VS DYNAMICAL STATE

Here, we compute a diagnostic of the dynamical state of halos as measured by the parameter $\eta = 2K/|U| - 1$, where K is the kinetic energy and U is an estimate of the potential energy of the halo. Values of $\eta \sim \mathcal{O}(1)$ are indicative of deviation from the virial theorem. For instance Neto et al. (2007) consider halos to be virialized if $\eta < 0.3$, while Ludlow et al. (2013) assume a more stringent criterion $\eta < 0.1$. Other proxies used in combination with η are the measure of the off-set between the peak density of the halo and its center of mass.

As pointed out in Section 4, while K is unambiguously defined

in terms of the halo particles (since it is given by the sum of the kinetic energy of all particles in the halo). In contrast U is a non-local quantity which is usually estimated by computing the potential energy between pairs of particles in the halo. However, this only gives a lower limit to the total potential energy since there could be non-negligible contributions from particles residing in the surrounding density field or nearby halos. This implies that results may strongly depend on the halo detection algorithm or the virial selection criteria.

In the upper panel of Figure B1 we plot the distribution of $\tilde{\chi}^2$ -values as function of η at $z = 0$ for the SO halos from the Λ CDM-W5 simulation with 512^3 particles and $162 h^{-1}$ Mpc boxlength. We can see that for the most massive halos ($M_{200} \gtrsim 2 \times 10^{14} h^{-1} M_{\odot}$) $\tilde{\chi}^2$ is an increasing function of η . If we assume halos to be virialized for $\eta < 0.3$ then there is a non-negligible fraction of halos which are more than 2σ from NFW ($\tilde{\chi}^2 \gtrsim 10$) and deviates from the virial condition. Instead if we consider the more stringent criterion $\eta < 0.1$ the fraction reduces accordingly. In any case the correlation remains difficult to assess because of a large scatter. This is not the case of FoF halos from the same simulation which are shown in the lower panel of Figure B1. Here, a correlation between $\tilde{\chi}^2$ and η clearly stands out for the most massive halos. We can see that a large fraction of them are more than 2σ from NFW ($\tilde{\chi}^2 \gtrsim 4$) while deviating from “equilibrium” even assuming a less conservative criterion $\eta < 0.3$.

The difference between SO and FoF analyses shows that it is far from trivial to establish the dynamical state of halos in absolute terms since the diagnostic critically depends on the halo detection algorithm and the selection criteria⁴.

This analysis indicates that the deviations from NFW are correlated with the dynamical state halos, but the significance of this remains difficult to assess, thus requiring a dedicated separate study that goes beyond the scope of the work presented here.

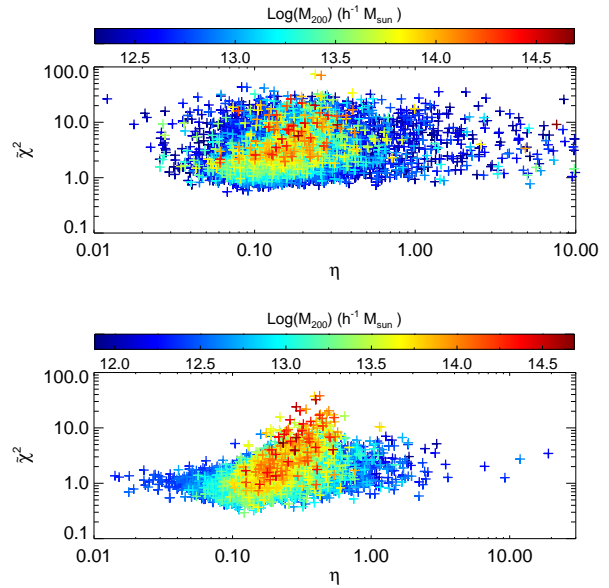


Figure B1. $\tilde{\chi}^2$ as function of η for SO (upper panel) and FoF (lower panel) halos at $z = 0$ from the Λ CDM-W5 simulation with 512^3 particles and $162 h^{-1}$ Mpc boxlength.

⁴ We find similar results for $\tilde{\chi}^2$ as function of the halo off-set which we do not show here.